



From Polymer to Magnetic Porous Carbon Spheres: Combined Microscopy, Spectroscopy, and Porosity Studies

Federico Cesano*, Sara Cravanzola, Valentina Brunella, Alessandro Damin and Domenica Scarano*

Department of Chemistry and NIS (Nanostructured Interfaces and Surfaces), Interdepartmental Centre and INSTM Centro di Riferimento, University of Torino, Torino, Italy

OPEN ACCESS

Edited by:

Alan Brian Dalton,
University of Sussex, United Kingdom

Reviewed by:

Feng Du,
Case Western Reserve University,
United States
Dimitrios Gournis,
University of Ioannina, Greece

*Correspondence:

Federico Cesano
federico.cesano@unito.it
Domenica Scarano
domenica.scarano@unito.it

Specialty section:

This article was submitted to
Carbon-Based Materials,
a section of the journal
Frontiers in Materials

Received: 07 October 2018

Accepted: 08 April 2019

Published: 08 May 2019

Citation:

Cesano F, Cravanzola S, Brunella V,
Damin A and Scarano D (2019) From
Polymer to Magnetic Porous Carbon
Spheres: Combined Microscopy,
Spectroscopy, and Porosity Studies.
Front. Mater. 6:84.
doi: 10.3389/fmats.2019.00084

The facile preparation of polymer waste-derived microporous carbon microspheres ($S_{\text{BET}} \sim 800 \text{ m}^2/\text{g}$) 100–300 μm in size, is reported at first. We have taken advantage of both, the crosslinked nature and the porous texture of the poly(4-ethylstyrene-co-divinylbenzene) microspheres, which allow the incoming anions and cations present in liquid media to enter and to remain segregated into the pores of the polymer microspheres as soon as the solvent is removed. Interestingly, the ZnCl_2 phase, when incorporated in the microporous molecular architecture of the polymer, prevents the collapsing of the pore structure of thermosetting polymer spheres during the pyrolysis occurring at 800°C and acts as an activating agent of the carbon phase under formation, being responsible for the formation of an extended meso- and macroporosity (30–200 and 300–1,000 Å ranges). More interestingly, porous carbon microspheres with magnetic properties have been prepared from the ZnCl_2 -activated porous carbon spheres after impregnation with Fe nitrate solution and thermal treatment at 800°C. A multi-technique methodology to characterize more extensively carbons at the micro/nanoscale is reported in the paper. More in detail, the morphology, structure, porous texture, and the surface properties of the carbon and of the magnetic carbon microspheres have been investigated by scanning and transmission electron microscopy, atomic force microscopy, X-ray diffraction, N_2 physisorption, diffuse reflectance UV-Vis, Raman and infrared spectroscopies. Furthermore, magnetic properties have been revealed at the nano- and at the macroscale by magnetic force microscopy and simple magnetically guided experiments by permanent magnets. The multi-technique methodology presented in the paper allows in elucidating more extensively about the different characteristics of activated carbons. Notwithstanding the huge amount of literature on activated carbons, the precise control of both the structure and the surface has, for the most part, hidden the relevance of other properties at the molecular scale of the assembled architectures. On the other hand, recent studies indicate that by molecular design, nanostructured, and porous carbonaceous materials could also be rationally proposed.

Keywords: Fe_3O_4 nanoparticles, magnetite, amorphous carbon, porous polymers, thermal activation, structure, textural properties, magnetic properties

INTRODUCTION

Porous activated carbon materials have attracted high interest in the past, due to their remarkable physical and chemical properties, including chemical inertness, mechanical stability, electrical conductivity, and biocompatibility (Lu et al., 2017; Wang et al., 2018). Activated carbons are now used in a broad range of industrial applications, including the gas/air cleaning from pollutants, and catalysis (Benzigar et al., 2018). Another field of application is the treatment/purification of liquids, like the water decontamination, which is of importance in the beverage, food, and pharmaceutical industries. More recent applications for C-doped systems have been also found in other fields, including energy fields and carbon capture (Calvo-Muñoz et al., 2016; Benzigar et al., 2018; Wang et al., 2018). In general, the choice of the most appropriate kind of activated carbon, for a specific use, depends primarily on its physical-chemical properties. When considering a material for such uses, the surface area, the pore-size, and the connectivity between the pores are by far the most relevant parameters. In order to tailor such specific properties, recent efforts have been made to design porous carbon materials with well-defined architectures, controllable pore size, and surface area (Borchardt et al., 2017).

As far as the size and shape control of the carbon materials is concerned, many porous carbons have been successfully obtained through templating methods using hard templates (Benzigar et al., 2018), such as mesoporous silica, zeolites and polymer microspheres, or soft templates, such as copolymer surfactants (Lu et al., 2017). Polymer spheres not only can allocate other systems (metal oxides and other structures in the porous channels) (Cesano et al., 2012a; Wang et al., 2018), but the formation of 3D ordered macroporous materials is promoted (Sadakane et al., 2010, 2012). Moreover, the templating routes have been used to synthesize hollow carbon spheres by coating a carbon precursor on a hard template core, which has been then removed (Liu et al., 2011) or by templated carbonization of glucose (Zhang et al., 2011), or of resorcinol-formaldehyde resins (Feather and Harris, 1973; Kraiwattanawong et al., 2011). The template fabrication of core-shell magnetic mesoporous carbon microspheres in 3-Dimensional ordered macroporous silicas has been also reported (Wang et al., 2014). In general, the preparation processes from the templating approaches are usually difficult and cost/time-consuming, which limit their practical applications (Lu et al., 2017). Notwithstanding feasible strategies may be adopted starting from cheaper material, such as polymer precursors (Cesano et al., 2012b; Fenoglio et al., 2015; Xu et al., 2017), biomaterials (Azevedo et al., 2007; Hadidi et al., 2017), and wastes (Franzoso et al., 2017; Nisticò et al., 2018) and performing simple processes, such as chemical and thermal treatments (Molina-Sabio and Rodriguez-Reinoso, 2004; Zhang et al., 2010; Rosas et al., 2014).

On the other hand, materials made by porous carbons together with inorganic compounds and oxides can be synthesized. Taken together, the two systems can show enhanced functionalities due to synergistic effects between multiple components, excellent performances in various fields, including biofuel cell, energy storage, fluorescent, or electronic biosensors

and as adsorbents (Cheng et al., 2014; Piñeiro-Prado et al., 2016). One useful example is that of the composite core-shell carbon spheres (Ag/C, Au/C) that have been obtained from the hydrothermal treatment of glucose (Sun and Li, 2004, 2005; Liu et al., 2011) and carbon nanospheres, 70-140 nm in size, obtained from cyclodextrins and maltodextrins (Shin et al., 2008; Zanetti et al., 2016; Anceschi et al., 2017). Meanwhile, the combination of carbon phases with oxides (TiO₂, ZnO, SnO₂, etc.) may offer a porous and nanostructured texture (Cesano et al., 2008a; Rahman et al., 2010) that makes the composite material catalytically photoactive under visible light (Cesano et al., 2008a, 2012a; Uddin et al., 2014; Cravanzola et al., 2015; Cravanzola et al., 2017).

Other useful examples to this context are those provided by carbons with magnetic properties. Colloidal and magnetic carbon spheres have drawn also particular attention because of their peculiar potential applications in catalysis (methanol oxidation) (Zhang et al., 2011), energy conversion and storage (Liu et al., 2011) (fuel cells, gas storage, and separation, and lithium-ion batteries; Yi et al., 2011), molecular adsorption/segregation (Liu et al., 2010; Yin et al., 2011; Lu et al., 2017).

Moreover, magnetic iron-based nanoclusters have been incorporated inside the hierarchical porous carbon microspheres to give to the obtained composites a magnetic separation property (Cesano et al., 2016; Lu et al., 2017). This provides a simple method to an easy removing and recycling of the adsorbents by means of an external magnet. Furthermore, multilayered structures made by porous carbon microspheres with embedded magnetic nanoparticles are known to show an enhanced high surface area, large pore volume together with superior adsorption capability, a fast adsorption rate and facile separation (Lu et al., 2017). The stability of magnetic nanoparticles is also greatly enhanced when they are covered by carbon layers, in a core-shell structure, thus preventing the nanoparticles from agglomeration phenomena (Jafari et al., 2014). Hence, by combining the advantages of cheap activated carbon and the properties of the magnetic particles, it is possible to fabricate new adsorbents incorporating iron-based particles, being the high surface area, the suitable pore size and the separability the main goals to achieve (Yang et al., 2008).

Herein, we report a simple method for fabricating magnetic carbon materials, moving from a copolymer of polystyrene and divinylbenzene (*PS-co-DVB*). Firstly, we demonstrate that microporous carbon spheres with controlled sizes and porous textures can be prepared from low-cost polymer waste, that is a commercially available, inexpensive and easy to handle resin. Secondly, the as-prepared spheres possess a large pore volume, a relatively high surface area and a wide mesopore size distribution, as obtained from gas sorption isotherms. Together with porosimetry and spectroscopies (Raman, FTIR and UV-Vis), microscopies (SEM, TEM, and AFM/MFM) provide a comprehensive multitechnique approach for the textural imagining. Lastly, the mesoporous carbon microspheres with magnetic properties can be produced after additional treatment with iron salt and annealing. Therefore, the present study suggests not only the higher-value use of polymer wastes and clarifies the relationship between the surface properties/porous

texture of the polymer-derived carbons, but, more interestingly, it highlights the fact that the mesoporous properties, together with the magnetic character of the hybrid carbon, can make it suitable for constructing multifunctional materials with magnetically driven processes. On the other hand, the topic of the molecular design of porous carbons, escaping from the simple concept of the structure/surface control, is of tremendous interest (Liu et al., 2015; Borchardt et al., 2017). Aiming to tailor and adjust the intrinsic characteristics (i.e., electrical conductivity, bandgap, enantioselectivity and other optical properties, interaction with specific guest molecules, etc.), the carbon materials with attained functionality can emerge in new application fields.

EXPERIMENTAL

Materials

ZnCl₂ has been dissolved in ethanol at 110°C (10:3 weight ratio of ZnCl₂), mixed to polymer in the 10:1 w/w and then stirred and dried at 80°C for 24 h, according to the preparation procedure of the carbon microspheres summarized in **Scheme 1**. Following this, the PS-co-DVB polymer microspheres either pure (**Scheme 1, Step A**) or containing ZnCl₂ salt as an activating agent (**Scheme 1, Step B1**) were produced as the result of the thermal treatment under N₂ gas flow up to 800°C for 5 h. Then, the ZnCl₂-activated carbon microspheres coming from **Step B1** have been impregnated with a 0.011 M ethanol solution of Fe(NO₃)₃ for 20 h at RT and thermal treated under N₂ gas flow up to 800°C for 5 h (**Scheme 1, Step B2**).

Methods

Microscopy and Structural Analysis

The microspheres were analyzed at the different steps of preparation. The morphology and the structure of the samples were investigated using scanning electron microscopy (SEM), transmission electron microscopy (TEM) and atomic force microscopy (AFM). More in detail, the images were taken on: (i) a Zeiss Evo 50 SEM instrument operating at 30 kV, (ii) a JEOL 3010-UHR HRTEM microscope operating at 300 kV, equipped with a 2 × 2 k pixels Gatan US1000 CCD camera, (iii) Nanosurf Easyscan2 AFM instrument, equipped with a 10 μm scan-head, high-performance anti-vibration platform in an acoustically insulated enclosure and Faraday cage. Reciprocal lattices and electron diffraction patterns were obtained by means of CaRine Crystallography 3.1 simulation package. Sections of the Fe-based microspheres were also obtained by adopting the ultramicrotomy method to explore the inner structure of the material. Briefly, microspheres magnetically guided to the bottommost region of an Eppendorf tube were embedded with the epoxy resin to constitute a block specimen, which is then cross-sectioned after curing. The thin microtomed slices, containing the cross-sections of the microsphere were obtained by using a regular gemgrade diamond knife. Samples were then investigated by SEM. Phase composition of microspheres was obtained by XRD analysis on a PANalytical X'Pert PRO diffractometer equipped with a Cu source and a Ni filter, in a standard Bragg–Brentano geometry. The profile fitting method in the whole XRD patterns has been adopted to determine the phase compositions and crystal

sizes (JADE 6.5, Materials Data). Vibrational properties were investigated by: (i) Renishaw inVia Raman microscope equipped with 785 nm (diode laser) and 514 nm (Ar⁺) laser-lines and (ii) Renishaw Raman InVia spectrophotometer with 442 nm laser-line. Raman spectra were collected by 20× objectives, <1 mW at the sample and with an in-house made rotating configuration to avoid sample heating and damaging (Signorile et al., 2018).

Porosity and Porous Texture Analysis

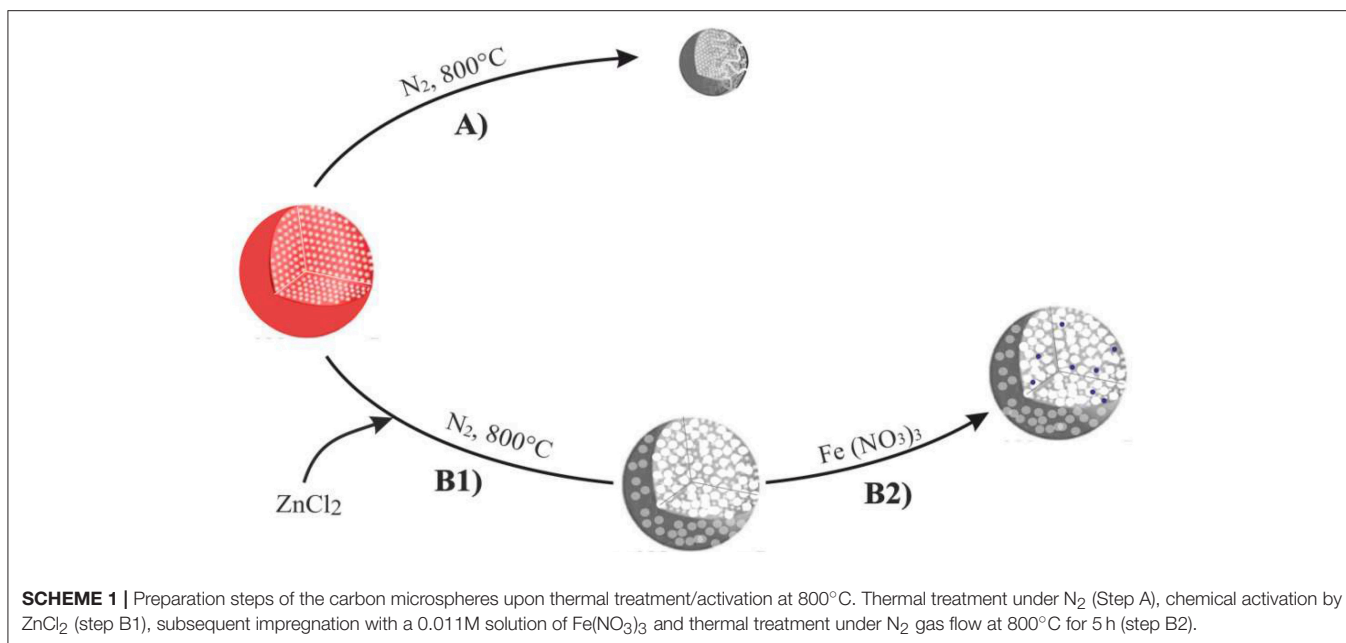
N₂-adsorption/desorption isotherms were obtained at 77 K (Micromeritics ASAP 2020 instrument) to determine the porosity properties of the materials at the different stages of preparation. Before analysis, the samples, as obtained following the before described procedure, were further outgassed overnight at RT (for the starting PS-co-DVB polymer) or at 400°C (for the resulting carbon materials after the thermal treatments). The surface area (S_{BET}) was calculated by the *Brunauer–Emmett–Teller* (BET) equation (in the relative pressure range of 0.05–0.25 p/p₀). Total pore volume was determined from the amount of N₂ adsorbed at the 0.98 p/p₀. Micropore surface area and volume were calculated from N₂ adsorption isotherms using the Carbon Black STSA *t-plot* equation. Mesopore volume (V_{meso}) was calculated by subtracting the micropore volume (V_{micro}) from the total pore volume (V_{tot}). The pore size distributions (PSDs) were derived from the N₂ adsorption isotherms using a non-negative least squares fitting on the adsorption isotherm data by applying the density functional theory (DFT) method (N₂-DFT model, slit geometry) by means of the MicroActive Datamaster 5 software (Micromeritics).

Investigation of Magnetic Properties

Magnetic force microscopy (MFM) images were obtained on a microtomed cross-section of a Fe-based microsphere in a dual-pass mode performed by using the same AFM equipment. The morphological properties were obtained in the intermittent contact mode during a first scan, while the MFM phase imaging was operated in the second scan, at constant-height (H) above the surface with the same magnetic probe (SSS-MFMR, Nanosensors; with a tip radius of 15 nm by using a resonant frequency of 75 kHz) without bias or external magnetic field applied, by monitoring the shifting of the phase and of the amplitude signals. The two scans allow to discriminate short (van der Waals, i.e., topography) and longer range (magnetic) interactions. The magnetic tip probe was magnetized by an external magnet (magnetization along the tip-axis) and tested on a magnetic grid prior to measurements.

Analysis of Spectroscopic Properties

The optical properties of the samples have been obtained by means of Diffuse Reflectance (DR) UV–vis–NIR spectrophotometer (Varian Cary UV 5000 equipped with a diffuse reflectance sphere) in the 14,000–40,000 cm⁻¹ range (about 700–250 nm wavelength range). The samples were diluted in BaSO₄ to provide detectable Kubelka–Munk values. FTIR spectra have been recorded on a Perkin Elmer Spectrum 100 in the attenuated total reflectance (ATR) mode with a diamond crystal and in the transmission mode on KBr pellets using 32



scans per spectrum with a resolution of 4 cm⁻¹ to detect the low wavenumber region (700–450 cm⁻¹ range).

Thermal Analysis

Thermogravimetric measurements (TGA, Q600-SDT TA instruments) were performed under air up to 800°C (heating rate 15°C/min) to quantify the iron oxide loading.

RESULTS AND DISCUSSION

Morphology, Structure, and Textural Properties of the Samples

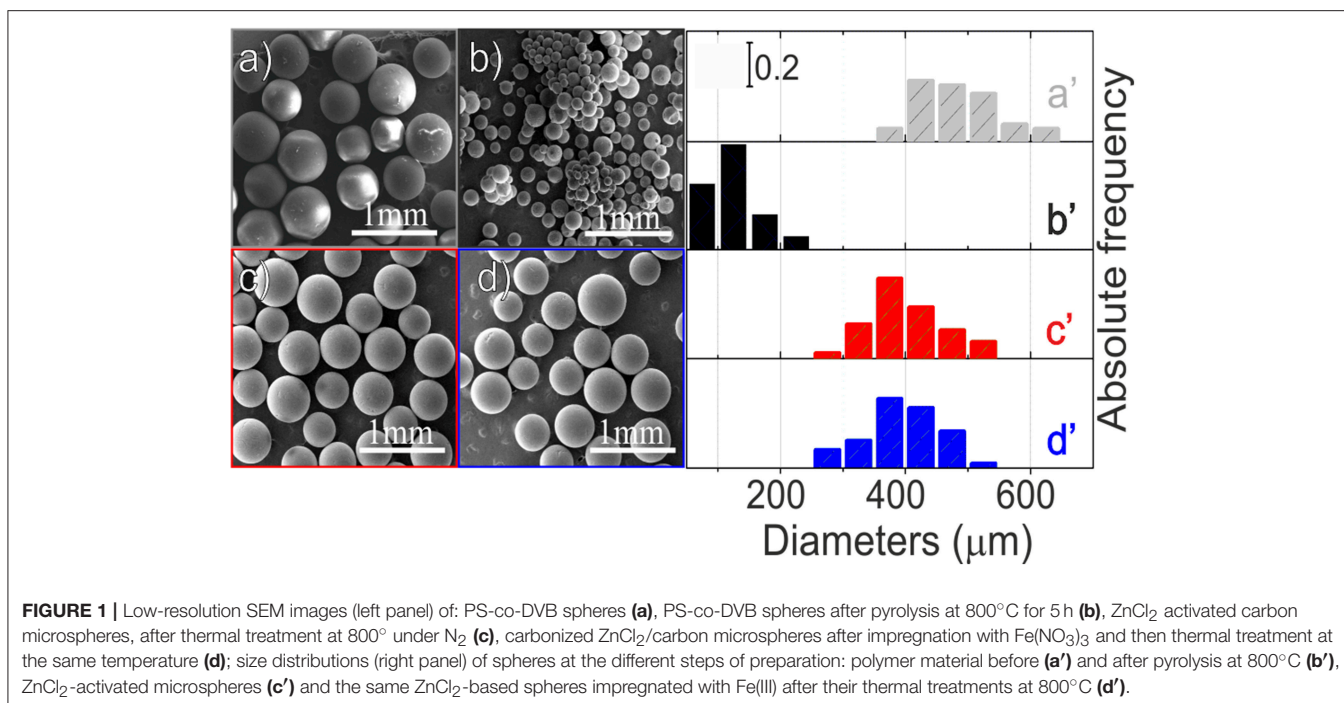
Low-resolution SEM images of the material at the different steps of preparation are shown in **Figures 1a–d** while the corresponding size distributions are illustrated in the right panel (**Figures 1a'–d'**).

From this figure, it is evident that, after the pyrolysis at 800°C (**Figure 1b**), the PS-co-DVB spheres maintain their spherical shape, but they are smaller in size, thus changing from 350–600 to <250 μm. Conversely, when the ZnCl₂-embedded polymer is taken under consideration, after the thermal treatment under N₂ gas flow at 800°C, the situation is completely different (**Figure 1c**). The sample is still formed by spherical particles, but their diameters, ranging in the 250–550 μm interval, are closer to those of the raw material spheres. Notice that the sizes are retained also after the thermally treated Fe(III)-impregnated carbon spheres (**Figure 1d**). From these images, the remarkable role of the embedded ZnCl₂ phase into the pores, in preserving the structure of the spheres upon the thermal treatment at 800°C under N₂ gas flow, can be highlighted. However, at this level of magnification, nothing more can be inferred.

SEM and AFM images of the raw copolymer and of the carbon spheres at the different steps of preparation are shown in

Figure 2. A polymer sphere, showing cracks and an apparently smoothed surface (SEM images in **Figures 2a,a'**), reveals its ultimate nature of assembled rounded domains, with sizes in the 0.1–0.3 μm range, as AFM imaged in **Figure 2a''**. Some copolymer spheres are SEM imaged after pyrolysis at 800°C for 5 h (**Figures 2b,b'**). Together with the before observed shrinkage of particles, also the rough surface, the occurrence of deep cracks, wrinkles, and folds at the surface, can be highlighted. Some more, from the AFM analysis, the assembling of the small nanoparticles is observed (**Figure 2b''**). ZnCl₂-embedded spheres are SEM and AFM imaged after the thermal treatment at 800°C for 5 h in **Figures 2c,c''**. An apparent flatter surface, interrupted by small cracks of irregular shape, is obtained at low resolution (**Figures 2c,c'**), but a more irregular morphology, made of uneven hills, relatively large folds and small grains, whose edges are reasonably responsible for the porosity, is shown at the nanometric scale (**Figure 2c''**). Similar considerations can be made for the thermally annealed ZnCl₂-embedded spheres after the impregnation with Fe nitrate, which behave in the same way as the sample before iron impregnation (**Figures 2d,d''**).

XRD patterns at the different steps of preparation are reported in **Figure 3**. In this figure, XRD patterns of the copolymer, either pure or with ZnCl₂, both after the thermal treatments at 800°C under N₂ gas flow for 5 h (black and red patterns, respectively), exhibit two very broad features. The first one, ranging in the 15° < 2θ < 30° range, can be assigned to the (002) plane reflections of sp²-C in the graphitic structure, whereas the very broad peak, in the 40° < 2θ < 50° range, can be assigned to the (10) band (a somehow convolution of the (100)/(101) XRD diffraction planes of the graphitic carbon) (Cesano et al., 2016). The wide character of these two features is typically observed in turbostratic stacking of carbon layers or more defective arrangements (amorphous carbons) (Wollbrink et al., 2016). The stacking order and the lateral size of the



crystallites along the XY-plane direction, estimated from the width of the (002) and of the (100) plane reflections by using the Scherrer equation, result to be of about 1.2 and 1.6 nm, respectively for all the carbon samples. Besides the before discussed XRD reflections, some additional peaks, although of low intensity, can be highlighted at $2\theta = 30.1^\circ$, at $2\theta = 35.4^\circ$, $2\theta = 43.0^\circ$, $2\theta = 53.4^\circ$, $2\theta = 56.9^\circ$, and at $2\theta = 63^\circ$ for the Fe (III) impregnated material after the thermal treatment (blue pattern). These XRD reflections can be carefully assigned to the (220), (311), (400), (422), (511), and (440) planes of magnetite-Fe₃O₄ (PDF card n. #019-0629). The mean crystallite sizes of the Fe₃O₄ nanoparticles result to be of about 12 nm by applying the Scherrer equation to the (311) plane reflection at 35.4° . The amount of the iron oxide inside the carbon spheres is however low (about 2.6 wt%, **Supplementary Figure 1**) and the coexistence with other Fe species, even at lower amounts, thus escaping from the XRD detection, cannot be ruled out. As the distinction between magnetite (Fe₃O₄) and maghemite (γ -Fe₂O₃), is usually very difficult, because of their very similar lattice parameters (Frison et al., 2013), particular care has been paid to the analysis of the XRD peak positions and shape in whole XRD pattern.

The N₂ adsorption/desorption isotherms and the pore size distributions of the porous spheres, at the different stages of preparation, are shown in **Figures 4a–c**, while the porosity properties are summarized in **Table 1**. The PS-co-DVB polymer (**Figure 4**, a-curve) exhibits a type-I isotherm with a long slope up to the relative pressure of about 0.3 p/p₀, which is indicative of a wide distribution of micropores and larger pores. The same kind of isotherm (type-I) is observed for the PS-co-DVB polymer pyrolyzed at 800°C (**Figure 4**, b-curve), which displays a more rectangular shape, associated with narrow micropores.

The relatively low N₂ uptake is also indicative of the smaller volume developed, being the pores too small to trap nitrogen. The partial collapsing of the carbon framework, occurred during the thermal process of the pure polymer phase, is confirmed by the reduction in the porosity. The situation is, however, completely different for the ZnCl₂-activated samples treated at the same temperature (800°C), before and after impregnation with Fe (III) and the subsequent thermal treatment (**Figure 4**, c and d-curves, respectively). The ZnCl₂-based pyrolyzed carbon materials display a combination of type I and type IV(a) isotherms with steep capillary condensation steps at the relative pressure from about 0.6 and 0.5 p/p₀ (ZnCl₂-treated and Fe-based ZnCl₂-treated samples, c- and d-curves, respectively), indicating the presence of both, well-developed micro- and mesoporosity. The shape of this hysteresis-loop is suggestive of a mixed H4/H1 type, which can be described with a different nature (Thommes et al., 2015), one more common for micro-mesoporous carbons developed by the isotherm at the lower pressure range and one with a more pronounced uptake at the high p/p₀, being the behavior associated with the occurrence of more larger and uniform meso/macropores (see steep capillary condensation at the higher relative pressure).

All these findings are in good agreement with the pore size distributions (PSDs) obtained by using the DFT model (**Figure 4**, right panel). Going into detail, the microporous polymer and carbon spheres, obtained from the direct thermal pyrolysis, show two families of micropores (<7 Å, minor; 9–13 Å range), while the carbonized ZnCl₂/PS-co-DVB spheres show a more complex distribution of pores. Besides the two families of micropores (ultramicro-pores, <6 and 11–15 Å), two additional families of meso- and meso/macropores, very wide in size (30–200 and 300–1,000 Å ranges), are shown. After the subsequent Fe (III)

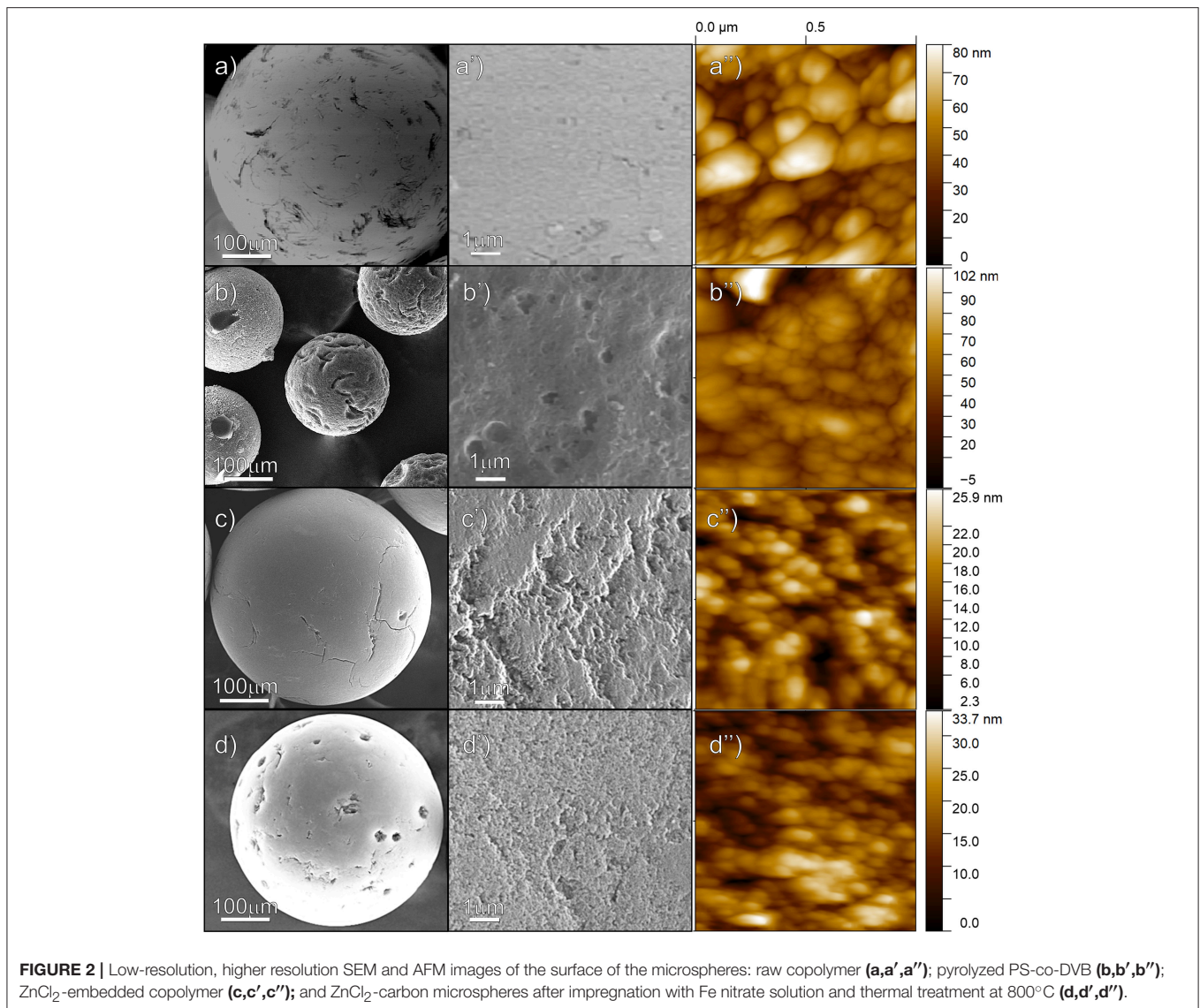


FIGURE 2 | Low-resolution, higher resolution SEM and AFM images of the surface of the microspheres: raw copolymer (**a,a'**); pyrolyzed PS-co-DVB (**b,b'**); ZnCl_2 -embedded copolymer (**c,c'**); and ZnCl_2 -carbon microspheres after impregnation with Fe nitrate solution and thermal treatment at 800°C (**d,d'**).

impregnation and thermal treatment at 800°C , no considerable modifications of the PSD are observed. Further differences can be highlighted from the porosity data (BET surface area: S_{BET} ; micropore volume: V_{micro} ; mesopore volume: V_{meso} ; and total pore volume: V_{tot}) of the samples, which are summarized in **Table 1**.

It is noteworthy that the ZnCl_2 dispersed in a polymer phase entails a set of reactions (i.e., melting, decomposition, oxidation, reduction to metal and vaporization), thus favoring the formation of an open porosity during the thermal treatment (Cesano et al., 2008b). Furthermore the formation of large mesopores has been observed when ZnCl_2 is molecularly dispersed in the thermosetting resins (Cesano et al., 2012b). Taking into consideration these previous studies, the fact that ZnCl_2 is effective not only in preserving the structural texture from the collapsing during the carbonization step, but also in the activation of the carbon phase under formation, is well-testified by the contribution of the larger pores (meso- and macropores),

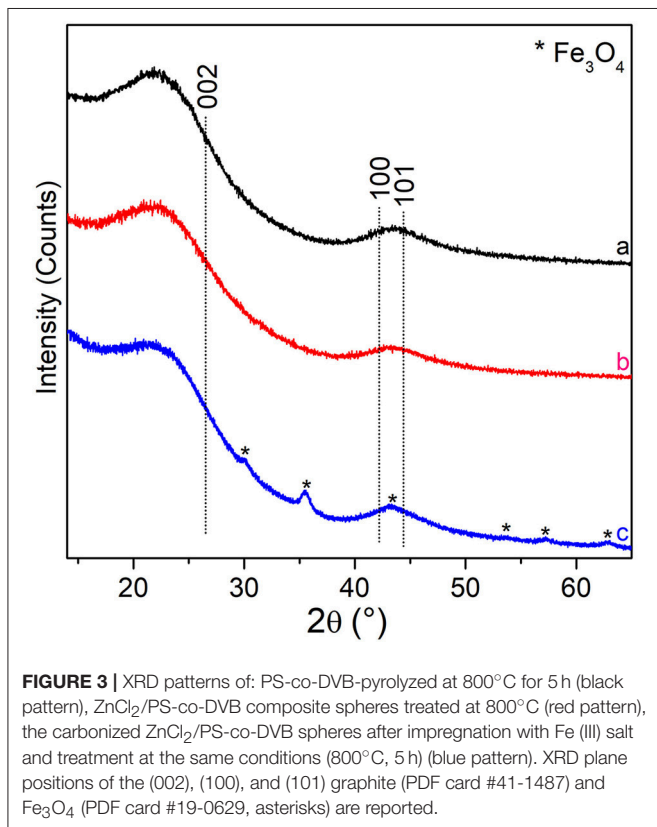
as well as of the total nitrogen uptake in the V_{tot} . The following impregnation of the so-obtained carbon microspheres slightly reduces the porosity, but does not affect the pore distributions in large amount.

Inner Structure, Textural, and Vibrational Properties of the Magnetite-Based Carbon Microspheres

A better understanding of the inner structure, in terms of porosity textures of the Fe_3O_4 -based carbon microspheres and of the nanoparticle distribution, has been further obtained by SEM and TEM analyses (**Figures 5a–d** and **Supplementary Figure 2**).

SEM image (**Figure 5a**) shows a section of the Fe-based carbon microsphere on a microtomed slice (see inset). From this image, pores of irregular shape and distribution with sizes in the 50–100 nm range are clearly shown, but nothing more can be inferred about the Fe phase(s), at the adopted resolution.

To gain more insights at the atomic scale, the sample has been TEM and HRTEM imaged, as shown in **Figures 5b–d**



and **Supplementary Figure 2**. Moving from **Figure 5b**, besides nanoparticles and aggregates well-dispersed in the matrix with sizes in the ~10–30 nm range, the macroporous nature of the scaffold can be illustrated, where a typical cross-sectional portion of an irregular shaped pore 100 × 200 nm in size is shown. The irregular morphology of the macropores (marked with 1, 2, 3) and of the mesopores about 10 nm in size (marked with 4, 5, 6), which are occurring as irregular voids between agglomerates, is further highlighted in **Figure 5c** and **Supplementary Figure 2**. Notice that the pore walls are mostly dominated by curved surfaces. Some more, from the **Figures 5c,d** regularly shaped nanoparticles and small nanoparticle aggregates, embedded in the carbon amorphous phase, can be better highlighted. In particular, two families of interference fringes, 2.53 Å spaced, can be assigned to the (311) planes of the magnetite nanoparticle

TABLE 1 | Surface area (m² g⁻¹) and pore volume (cm³ g⁻¹) of the materials at different stages of preparation.

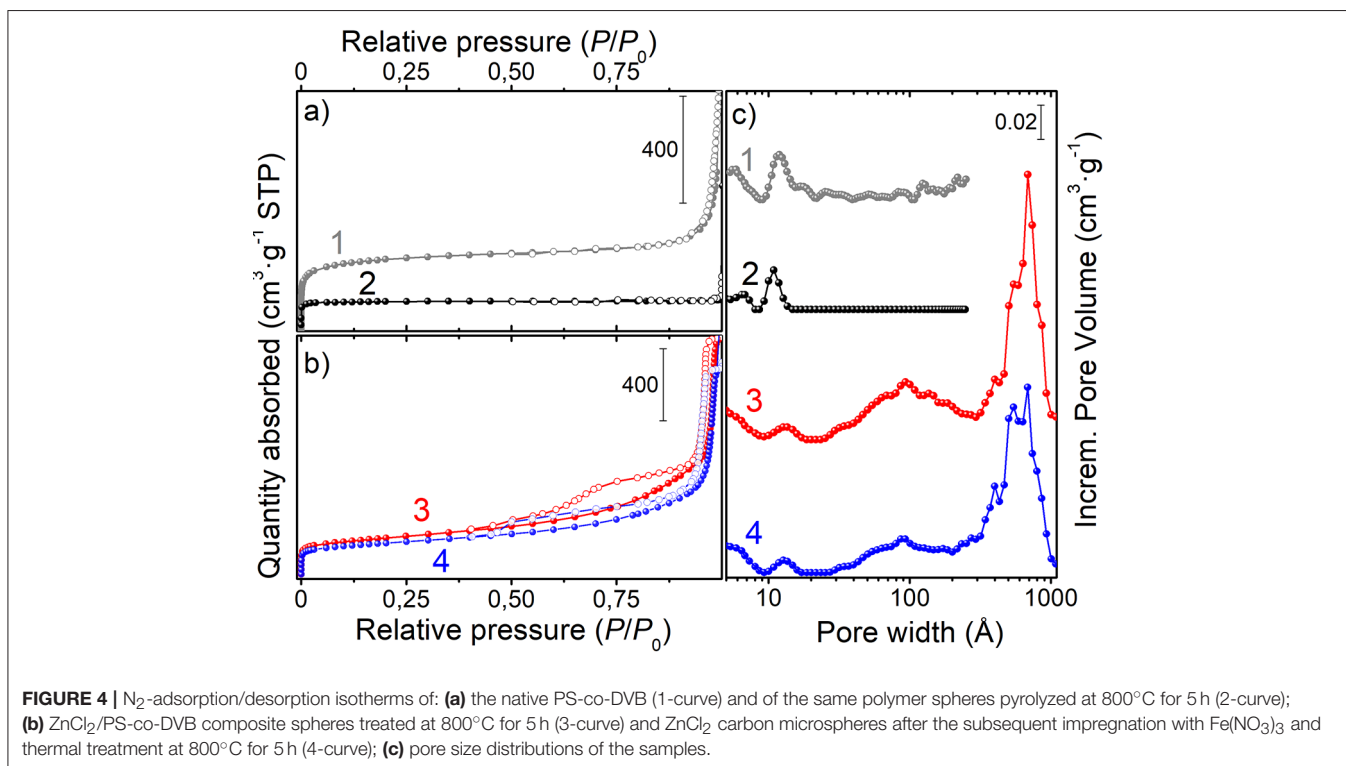
	S _{BET} ^a	V _{tot} ^b	V _{micro} ^c	V _{meso} ^d	V _{meso} (%)
PS-co-DVB	930	0.7732	0.3859	0.3873	50
PS-co-DVB@800°C	386	0.1799	0.1727	0.007	4
ZnCl ₂ /PS-co-DVB@800°C	807	1.7136	0.1591	1.5545	91
Fe-based	702	1.5342	0.1497	1.3876	90
ZnCl ₂ /PS-co-DVB@800°C					

^aTotal area evaluated following the BET model in the standard 0.05 < P/P₀ < 0.25 pressure range.

^bTotal pore volume calculated as volume of the liquid at p/p₀ ≈ 0.98.

^cV_{micro} calculated by using t-plot method (Harkins and Jura or Carbon Black STSA thickness equations for PS-co-DVB or the thermally treated samples, respectively).

^dV_{meso} = V_{tot} - V_{micro}.



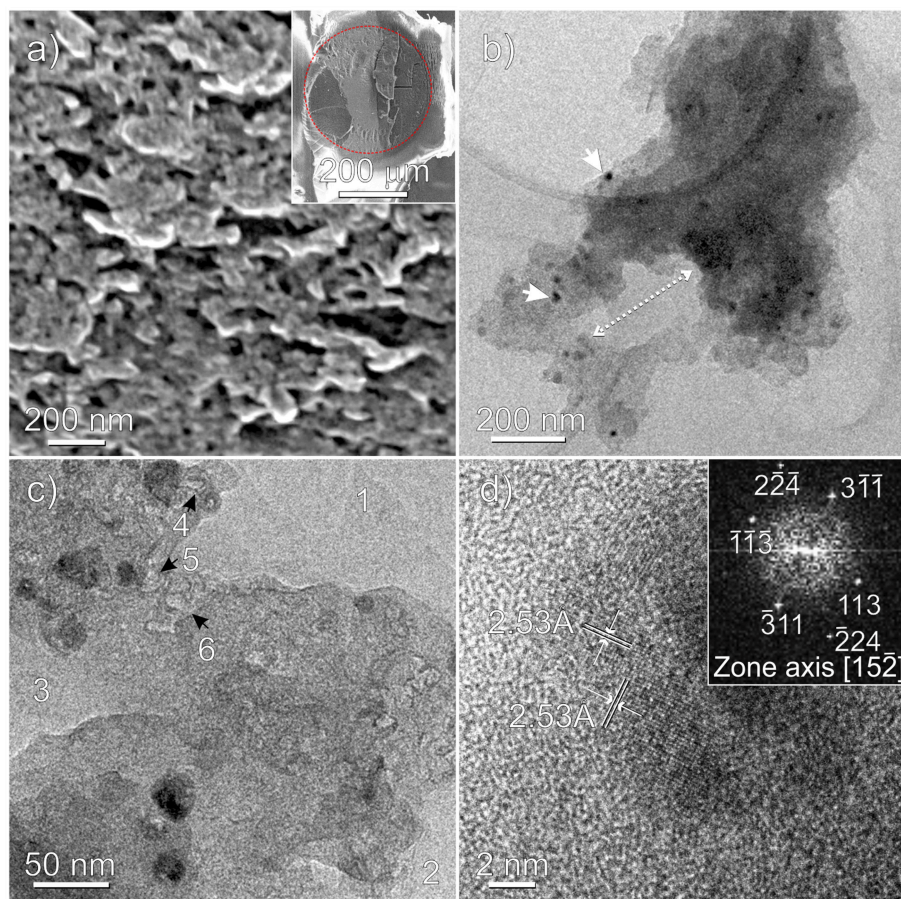


FIGURE 5 | Fe_3O_4 -based $\text{ZnCl}_2/\text{PS-co-DVB}$ microspheres treated at 800°C : HRSEM (a), TEM (b,c), and HRTEM (d) images. A thin slice of a microsphere embedded in the epoxy resin after sectioning the specimen by ultramicrotomy is shown in the inset of (a). The red dotted line evidences the embedded carbonaceous microsphere (darker region) from the epoxy resin (brighter region). Nanoparticles and macropores are highlighted in (b), while 1, 2, 3 and 4, 5, 6 refer to macro- and mesopores in (c), respectively. In the inset of (d) the selected nanoparticle is FFT imaged.

encapsulated in the porous carbon matrix (**Figure 5d**). To this regard, the observed symmetry and the spacings of the bright spots on the FFT (fast Fourier transform) image (inset of **Figure 5d**) are well-compatible with the orientation along $[1\ 5\ -2]$ zone axis of the Fe_3O_4 nanoparticle (**Supplementary Figure 3**). Nonetheless, the presence of other Fe phases (i.e., maghemite) into the sample cannot be ruled out. We shall return on this point by comparing AFM and MFM images of the obtained samples. By now, it is worthy noticing that, together with SEM, the TEM analysis has a relevant role in investigating the porosity of the sample at the nanometric scale, well-supporting the results obtained by gas sorption techniques, which on the other hand provide a systematic statistical analysis. Conversely, due to the distinctive feature of the microscopy approach that is local, and then not statistical, TEM would be ineffective without porosimetry analysis.

Raman spectra of magnetic carbon microspheres, obtained by means of three laser lines (785, 514, and 442 nm), are displayed in **Figure 6**. All the spectra are dominated by two

intense bands, attributed to vibrational modes involving sp^2 -carbon species with a low sp^3 -carbon content commonly found in defective nanographitic crystallites (Ferrari and Robertson, 2000; Pimenta et al., 2007; Groppo et al., 2018). The signal around $1,600\ \text{cm}^{-1}$ (G-band, E_{2g} symmetry), resulting from the in-plane bond stretching, is for a fact upward shifted of about $20\ \text{cm}^{-1}$ with respect to the G-band of graphite, thus indicating that the stacking order of the sheets is very low and that the structure is also defective. The second foremost feature around $1,350\ \text{cm}^{-1}$ (D-band, A_{1g} symmetry), that is forbidden in the perfect graphite, becomes active in presence of defects and is linked to the breathing modes of 6-membered carbon rings, being its position influenced by the excitation energy (inset of **Figure 6**). A D-band dispersion of about $42\ \text{cm}^{-1}/\text{eV}$ (slope of the linear fitting of D-band positions) is observed by varying the laser excitation energy in the visible range that is indicative of very small graphitic domains (L_a), which have been calculated to be about 14–15 nm given the proportionality $I_D/I_G \propto c'(\lambda) \times L_a^2$ (where $c' \sim 0.0055$ for $\lambda = 514\ \text{nm}$) (Ferrari and Robertson, 2000) and by using

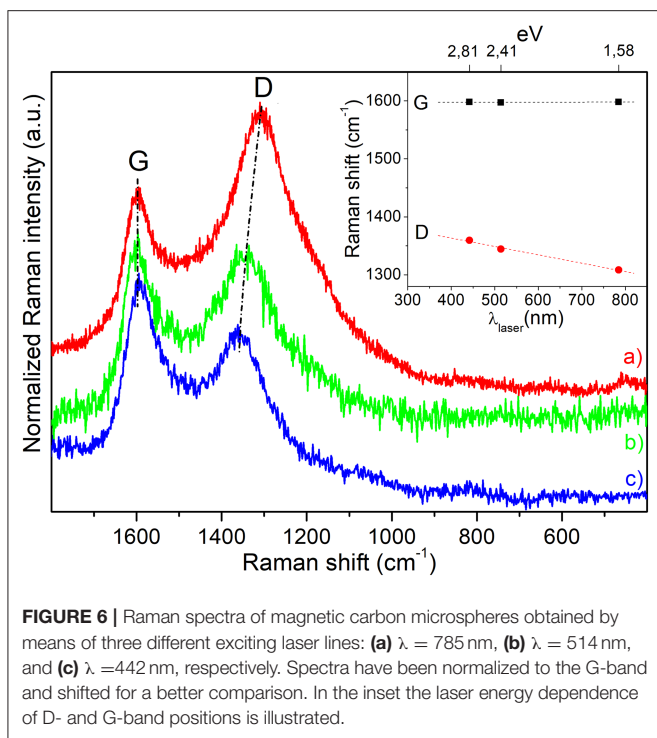


FIGURE 6 | Raman spectra of magnetic carbon microspheres obtained by means of three different exciting laser lines: (a) $\lambda = 785$ nm, (b) $\lambda = 514$ nm, and (c) $\lambda = 442$ nm, respectively. Spectra have been normalized to the G-band and shifted for a better comparison. In the inset the laser energy dependence of D- and G-band positions is illustrated.

the equation¹: L_a (nm) = $2.4 \times 10^{-10} \times (\lambda_{\text{laser}})^4 \times (I_D/I_G)^{-1}$ (Pimenta et al., 2007), where the λ_{laser} is in nm, I_D and I_G are the observed intensities of the D- and G-bands. It is worth noticing that the black color of the sample (Supplementary Figure 5) is responsible for the almost complete light absorption and the low quantity of Fe_3O_4 (~2.5 wt%) do not allow to recognize the magnetite vibrational fingerprints.

Magnetic Properties of the Fe_3O_4 -Based Carbon Microspheres

The combined AFM/MFM investigation of a Fe_3O_4 -based carbon microsphere is reported in Figure 7. Both the AFM topography and the related phase signal images, which are acquired with the standard intermittent contact mode by means of a first-pass acquisition, well-resemble the surface morphology (Figures 7a,b, respectively). The MFM phase shifting of the same region (Figure 7c) is obtained in a second scan above the sample surface to separately measure the magnetic properties after minimizing the capacitive tip-sample coupling (i.e., positive phase shift of non-magnetic interactions) by using a very sharp probe (Krivcov et al., 2018). From the MFM phase image obtained at $H = 60$ nm, the presence of magnetic material is demonstrated by the negative phase shifting (more extended dark domains), not affected by topography and associated with the attractive interactions between the tip and the sample (Nisticò et al., 2017, 2018).

¹Or L_a (nm) = $560/(E_{\text{laser}})^4 \times (I_D/I_G)^{-1}$, where E_{laser} is given in eV.

It is worthy noticing that, due to the good dispersion of the magnetic particles within the porous material (see TEM images), only the magnetic nanoparticles closer to the surface are expected to respond to the magnetic interaction with the tip probe.

In conclusion, from either the MFM signal and the TEM images, it results that the nanoparticles are mostly single domain particles or small aggregates of magnetic particles (Butler and Banerjee, 1975), but nothing more can be said about the orientation of their magnetic walls.

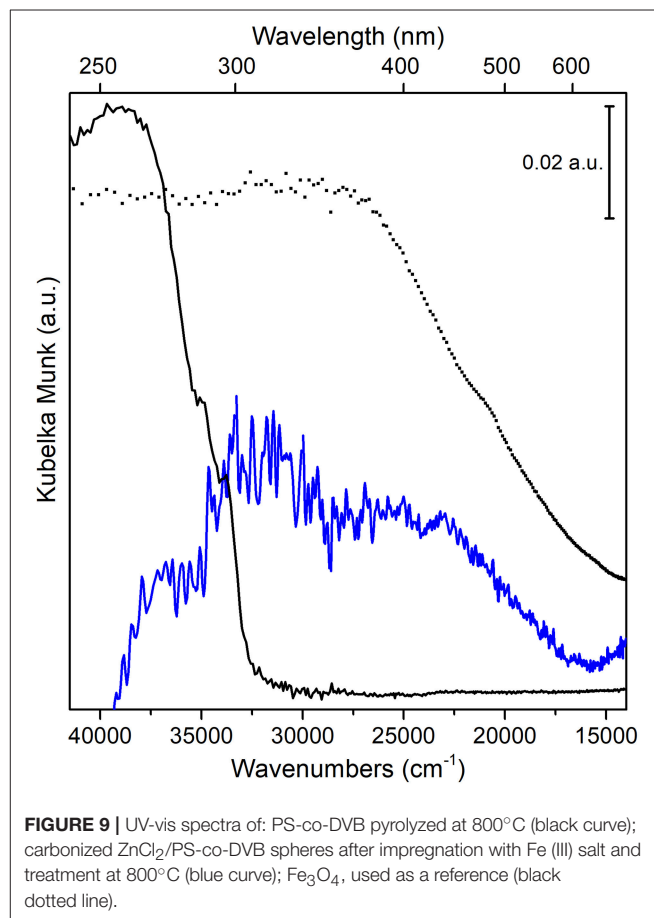
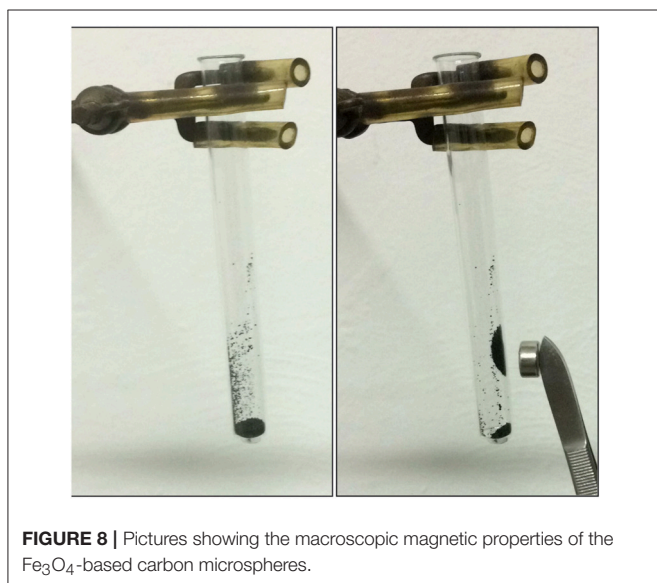
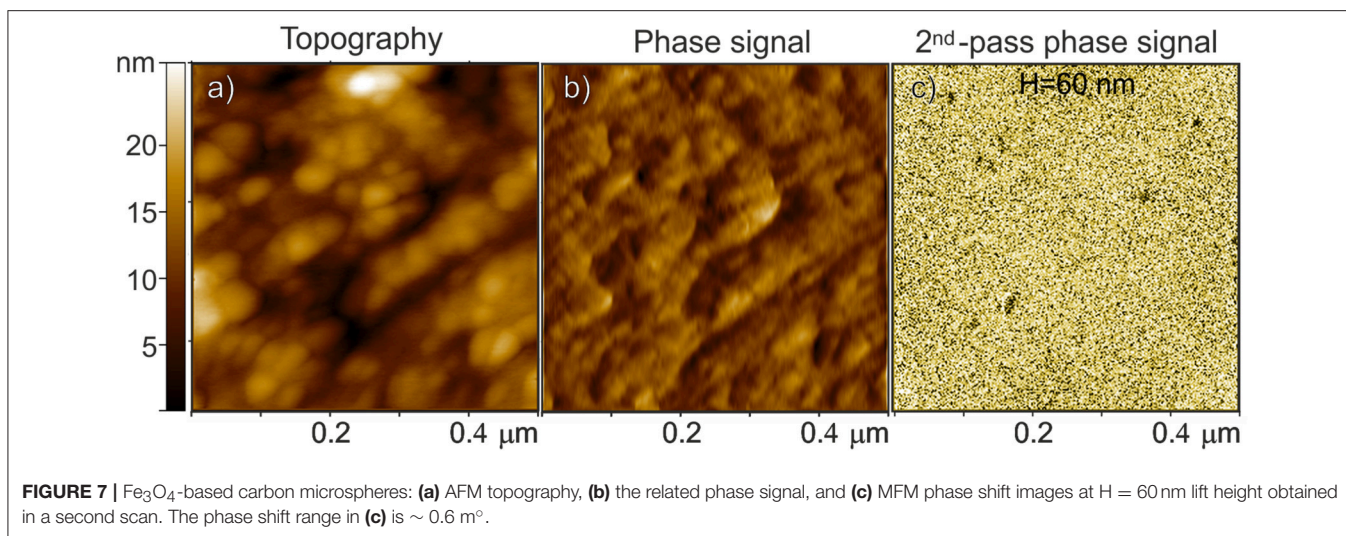
To investigate the macroscopic magnetic properties of the Fe_3O_4 -based carbon microspheres, a simple experiment was performed, as illustrated in Figure 8 and in Supplementary Video 1. From these it comes out that iron oxide-based carbon microspheres are affected by a hand-held external magnet.

Optical Properties of the Samples

The absorption spectra, in the 39,500–14,000 cm^{-1} (or 253–714 nm) UV-visible region, of PS-co-DVB-pyrolyzed at 800°C for 5 h (black curve), of the carbonized $\text{ZnCl}_2/\text{PS-co-DVB}$ spheres after impregnation with Fe (III) salt and treatment at the same conditions (800°C, 5 h) (blue curve), together with the Fe_3O_4 reference (Sigma Aldrich) (dotted curve) are compared in Figure 9.

The intense and wide absorption in the 38,000–33,000 cm^{-1} range (PS-co-DVB pyrolyzed at 800°C, black curve) can be assigned to the sp^2 trigonal π - π^* transitions of the amorphous carbon phase, as confirmed by IR results (see Supplementary Figure 4) (Applin et al., 2018). The observed broadening is presumably due to the larger distribution of bonding distances as a consequence of amorphisation effects, which is causing the π - π^* band to move to longer wavelengths too. The amorphous nature of the carbon structure for both carbon materials is also well-supported by the observed IR absorption band in the 1,620–1,450 cm^{-1} range, with a maximum at about 1,570 cm^{-1} (Supplementary Figure 4, left panel). Such IR band is, for a fact, associated with presence of double-conjugated C vibrational modes ($\nu_{\text{C}=\text{C}}$) in sp^2 carbons in presence of defects (i.e., surface terminations, heteroatoms, functional groups, radical species, where there is a change of the dipole moment (in contrast to what observed in graphitic carbon materials, more ordered domains) (Jain et al., 2017; Groppo et al., 2018).

Moving to Fe_3O_4 doped carbon sample (blue curve) and to Fe_3O_4 reference (dotted curve), at first a complex and featureless absorption, covering the 36,000–15,000 cm^{-1} interval, can be observed. Although it is quite difficult to resolve and then to assign the different transitions, according to some authors (He et al., 2005; Yang et al., 2015), we can state that inter-valence charge transfer (IVCT) transitions due to electron transfers from one cation to a neighboring cation in a different oxidation state, dominate the whole spectral region. Concerning Fe_3O_4 phase, this can be explained with transitions from Fe^{2+} to Fe^{3+} bonding and antibonding orbitals (t_{2g} , e_g in octahedral sites and t_2 , e in tetrahedral sites)



mediated by O^{2-} ions across the shared edges of adjacent Fe-O polyhedral (Fontijn et al., 1999).

Some more, besides IVCT, also pair excitations resulting from magnetic coupling between neighboring Fe^{3+} ions together with charge transfers from Fe^{3+} ions to the adjacent O^{2-} ions contribute to the broad and intense absorption of Fe_3O_4 nanoparticles in the $25,000\text{--}16,000\text{ cm}^{-1}$ interval. This behavior, typical of systems with two different oxidation states, is indicative of electron delocalization phenomena, which are responsible for the intense color of the material in the visible region as well. A further confirmation of the iron-based oxide formation comes from FTIR spectra, where the intense absorption in the $550\text{--}500\text{ cm}^{-1}$ interval, has been assigned to Fe-O stretching mode of Fe_3O_4 (Jafari et al., 2014) (Supplementary Figure 4, right panel).

Notice that the intense absorption at about $38,000\text{ cm}^{-1}$ (black curve), before ascribed to $\pi\text{-}\pi^*$ transitions of sp^2 carbon sites inside the amorphous carbon phase, is quite completely eroded, although a redshift inside the complex envelope cannot be ruled out (blue curve). From

this, one might infer the occurrence of Fe₃O₄/carbon interactions at the core-shell interface, as reported by some authors (Jafari et al., 2014).

It is worth noticing that, despite the fact that carbonaceous species are spectrally active in the ultraviolet (UV) region of the spectrum, they have been largely considered only for extra-terrestrial investigations and not for solar system surfaces up to now (Hendrix et al., 2016; Applin et al., 2018).

SUMMARY AND CONCLUSIONS

The attention on the precise control of the structure/surface has, for the most part, hidden so far the relevance of some properties related to the assembled architectures of the carbon materials. In accordance with the molecular design concept, the rational design of nanostructured porous carbonaceous materials has been adopted. In this contest, we have shown that polymer waste-derived microporous carbon microspheres ($S_{\text{BET}} \sim 800 \text{ m}^2/\text{g}$) 100–300 μm in size can be obtained by taking advantage of both, the crosslinked nature and the porous texture of the poly(4-ethylstyrene-co-divinylbenzene) precursor infiltrated by ZnCl₂. The ZnCl₂ phase, incorporated in the microporous scaffold of the polymer, prevents the collapsing of the pore structure and acts as an activating agent of the carbon phase under formation during the pyrolysis occurring at 800°C, so developing an extended mesoporosity. More interestingly, porous carbon microspheres with magnetic properties have been obtained from the ZnCl₂-activated porous carbon spheres after impregnation with Fe nitrate solution and thermal treatment at 800°C. A multi-technique approach has been adopted to characterize more extensively the carbons at the micro/nanoscale. In more detail, the morphology, structure, porous texture and the surface properties of materials have been investigated by several techniques (scanning and transmission electron microscopy, atomic force microscopy, X-ray diffraction, N₂-physisorption, diffuse reflectance UV-vis, and infrared spectroscopies). Moreover, magnetic properties have been shown at the nano- and at the macroscale by magnetic force microscopy and simple magnetically guided

experiments by permanent magnets. The presented multi-technique methodology aims also to an extensive description of the different characteristics of activated carbons with magnetic properties. The knowledge, tailoring of some intrinsic characteristics (i.e., surface chemistry, enantioselectivity, and other optical properties.) and the combination with some other functionalities (i.e., electrical, magnetic properties), can open a perspective unattainable for the more traditional materials.

AUTHOR CONTRIBUTIONS

FC, SC, AD, and VB conceived, designed, and performed the experiments and characterizations, analyzed the data. FC, SC, AD, and DS wrote the manuscript. All authors participated in the final editing of the manuscript, read and approved the paper.

FUNDING

This work was supported by MIUR (Ministero dell'Istruzione, dell'Università e della Ricerca), INSTM Consorzio, and NIS (Nanostructured Interfaces and Surfaces) Inter-Departmental Centre of University of Torino.

ACKNOWLEDGMENTS

The authors thank Dr. M. C. Valsania for the precious support in TEM experiments. Compagnia di San Paolo and University of Turin, through the program 2013–2015 (Open Access Raman Laboratory), are gratefully acknowledged.

SUPPLEMENTARY MATERIAL

The Supplementary Material for this article can be found online at: <https://www.frontiersin.org/articles/10.3389/fmats.2019.00084/full#supplementary-material> (TGA plot, additional SEM and TEM images, IR spectra, optical microscope images and a video demonstrating the macroscopic magnetic properties of the Fe₃O₄-based carbon microspheres).

REFERENCES

- Anceschi, A., Magnacca, G., Trotta, F., and Zanetti, M. (2017). Preparation and characterization of microporous carbon spheres from high amylose pea maltodextrin. *RSC Adv.* 7, 36117–36123. doi: 10.1039/C7RA05343F
- Applin, D. M., Izawa, M. R. M., Cloutis, E. A., Gillis-Davis, J. J., Pitman, K. M., Roush, T. L., et al. (2018). Ultraviolet spectral reflectance of carbonaceous materials. *Icarus* 307, 40–82. doi: 10.1016/j.icarus.2018.02.012
- Azevedo, D. C. S., Araújo, J. C. S., Bastos-Neto, M., Torres, A. E. B., Jaguaribe, E. F., and Cavalcante, C. L. (2007). Microporous activated carbon prepared from coconut shells using chemical activation with zinc chloride. *Microporous Mesoporous Mater.* 100, 361–364. doi: 10.1016/j.micromeso.2006.11.024
- Benzigar, M. R., Talapaneni, S. N., Joseph, S., Ramadass, K., Singh, G., Scaranto, J., et al. (2018). Recent advances in functionalized micro and mesoporous carbon materials: synthesis and applications. *Chem. Soc. Rev.* 47, 2680–2721. doi: 10.1039/C7CS00787F
- Borchardt, L., Zhu, Q.-L., Casco, M. E., Berger, R., Zhuang, X., Kaskel, S., et al. (2017). Toward a molecular design of porous carbon materials. *Mater. Today* 20, 592–610. doi: 10.1016/j.mattod.2017.06.002
- Butler, R. F., and Banerjee, S. K. (1975). Theoretical single-domain grain size range in magnetite and titanomagnetite. *Solid Earth Planets* 80, 4049–4058. doi: 10.1029/JB080i029p04049
- Calvo-Muñoz, E. M. J., García-Mateos, F., Rosas, J. M., Rodríguez-Mirasol, J., and Cordero, T. (2016). Biomass waste carbon materials as adsorbents for CO₂ capture under post-combustion conditions. *Front. Mater.* 3:23. doi: 10.3389/fmats.2016.00023
- Cesano, F., Bertarione, S., Damin, A., Agostini, G., Usseglio, S., Vitillo, J. G., et al. (2008a). Oriented TiO₂ nanostructured pillar arrays: synthesis and characterization. *Adv. Mater.* 20, 3342–3348. doi: 10.1002/adma.200702768
- Cesano, F., Pellerej, D., Scarano, D., Ricchiardi, G., and Zecchina, A. (2012a). Radially organized pillars of TiO₂ nanoparticles: synthesis, characterization

- and photocatalytic tests. *J. Photochem. Photobiol. A Chem.* 242, 51–58. doi: 10.1016/j.jphotochem.2012.05.020
- Cesano, F., Rahman, M. M., Bardelli, F., Damin, A., and Scarano, D. (2016). Magnetic hybrid carbon via graphitization of polystyrene-co-divinylbenzene: morphology, structure and adsorption properties. *ChemistrySelect* 1, 2536–2541. doi: 10.1002/slct.201600278
- Cesano, F., Rahman, M. M., Bertarione, S., Vitillo, J. G., Scarano, D., and Zecchina, A. (2012b). Preparation and adsorption properties of activated porous carbons obtained using volatile zinc templating phases. *Carbon* 50, 2047–2051. doi: 10.1016/j.carbon.2011.12.015
- Cesano, F., Scarano, D., Bertarione, S., Bonino, F., Damin, A., Bordiga, S., et al. (2008b). Synthesis of ZnO-carbon composites and imprinted carbon by the pyrolysis of ZnCl₂-catalyzed furfuryl alcohol polymers. *J. Photochem. Photobiol. A Chem.* 196, 143–153. doi: 10.1016/j.jphotochem.2007.07.033
- Cheng, G., Zhou, M.-D., and Zheng, S.-Y. (2014). Facile synthesis of magnetic mesoporous hollow carbon microspheres for rapid capture of low-concentration peptides. *ACS Appl. Mater. Interfaces* 6, 12719–12728. doi: 10.1021/am502712a
- Cravanzola, S., Cesano, F., Gaziano, F., and Scarano, D. (2017). Carbon domains on MoS₂/TiO₂ system via catalytic acetylene oligomerization: synthesis, structure, and surface properties. *Front. Chem.* 5:91. doi: 10.3389/fchem.2017.00091
- Cravanzola, S., Jain, S. M., Cesano, F., Damin, A., and Scarano, D. (2015). Development of a multifunctional TiO₂/MWCNT hybrid composite grafted on a stainless steel grating. *RSC Adv.* 5, 103255–103264. doi: 10.1039/C5RA15003E
- Feather, M. S., and Harris, J. F. (1973). Dehydration reactions of carbohydrates. *Adv. Carbohydr. Chem. Biochem.* 28, 161–224. doi: 10.1016/S0065-2318(08)60383-2
- Fenoglio, G., Carlos, L., and Nisticò, R. (2015). One-step synthesis of magnetic chitosan polymer composite films. *Appl. Surf. Sci.* 345, 175–181. doi: 10.1016/j.apsusc.2015.03.154
- Ferrari, A. C., and Robertson, J. (2000). Interpretation of Raman spectra of disordered and amorphous carbon. *Phys. Rev. B* 61:074414. doi: 10.1103/PhysRevB.61.14095
- Fontijn, W. F. J., van der Zaag, P. J., Feiner, L. F., Metselaar, R., and Devillers, M. A. C. (1999). A consistent interpretation of the magneto-optical spectra of spinel type ferrites (invited). *J. Appl. Phys.* 85, 5100–5105. doi: 10.1063/1.369091
- Franzoso, F., Nisticò, R., Cesano, F., Corazzari, I., Turci, F., Scarano, D., et al. (2017). Biowaste-derived substances as a tool for obtaining magnet-sensitive materials for environmental applications in wastewater treatments. *Chem. Eng. J.* 310, 307–316. doi: 10.1016/j.cej.2016.10.120
- Frison, R., Cernuto, G., Cervellino, A., Zaharko, O., Colonna, G. M., Guagliardi, A., et al. (2013). Magnetite-maghemite nanoparticles in the 5–15 nm range: correlating the core-shell composition and the surface structure to the magnetic properties. A total scattering study. *Chem. Mater.* 25, 4820–4827. doi: 10.1021/cm403360f
- Grosso, E., Bonino, F., Cesano, F., Damin, A., and Manzoli, M. (2018). “Raman, IR and INS characterization of functionalized carbon materials,” in *Metal-free Functionalized Carbons in Catalysis: Synthesis, Characterization and Applications*, eds A. Villa and N. Dimitratos (Cambridge: Royal Society of Chemistry), 103–137.
- Hadidi, L., Mahmoud, A., Purkait, T., McDermott, M., and Veinot, J. (2017). Cellulose nanocrystal-derived hollow mesoporous carbon spheres and their application as a metal-free catalyst. *Nanotechnology* 28:505606. doi: 10.1088/1361-6528/aa95a2
- He, Y. P., Miao, Y. M., Li, C. R., Wang, S. Q., Cao, L., Xie, S. S., et al. (2005). Size and structure effect on optical transitions of iron oxide nanocrystals. *Phys. Rev. B* 71:125411. doi: 10.1103/PhysRevB.71.125411
- Hendrix, A. R., Vilas, F., and Li, J. Y. (2016). The UV signature of carbon in the solar system Amanda. *Meteor. Planet. Sci.* 51, 105–115. doi: 10.1111/maps.12575
- Jafari, A., Boustani, K., and Farjami, S. (2014). Effect of carbon-shell on the structural and magnetic properties of Fe₃O₄ supermagnetic nanoparticles. *J. Supercond. Nov. Magn.* 7, 187–194. doi: 10.1007/s10948-013-2239-8
- Jain, S. M., Cesano, F., Scarano, D., and Edvinsson, T. (2017). Resonance Raman and IR spectroscopy of aligned carbon nanotube arrays with extremely narrow diameters prepared with molecular catalysts on steel substrates. *PCCP* 19, 30667–30674. doi: 10.1039/C7CP06973A
- Kraiwananawong, K., Sano, N., and Tamon, H. (2011). Low-cost production of mesoporous carbon/carbon composite cryogels. *Carbon* 49, 3404–3411. doi: 10.1016/j.carbon.2011.04.018
- Krivcov, A., Junkers, T., and Möbius, H. (2018). Understanding electrostatic and magnetic forces in magnetic force microscopy: towards single uperparamagnetic nanoparticle resolution. *J. Phys. Commun.* 2:075019. doi: 10.1088/2399-6528/aaad3a4
- Liu, J., Wickramaratne, N. P., Qiao, S. Z., and Jaroniec, M. (2015). Molecular-based design and emerging applications of nanoporous carbon spheres. *Nat. Mater.* 14, 763–774. doi: 10.1038/nmat4317
- Liu, R., Mahurin, S. M., Li, C., Unocic, R. R., Idrobo, J. C., Gao, H., et al. (2011). Dopamine as a carbon source: the controlled synthesis of hollow carbon spheres and yolk-structured carbon nanocomposites. *Angew. Chem. Int. Edn.* 50, 6799–6802. doi: 10.1002/anie.201102070
- Liu, Y., Ren, Z., Wei, Y., Jiang, B., Feng, S., Zhang, L., et al. (2010). Synthesis and applications of graphite carbon sphere with uniformly distributed magnetic Fe₃O₄ nanoparticles (MGCSs) and MGCS@Ag, MGCS@TiO₂. *J. Mater. Chem.* 20, 4802–4808. doi: 10.1039/b925706c
- Lu, F., Huang, C., You, L., Wang, J., and Zhang, Q. (2017). Magnetic hollow carbon microspheres as a reusable adsorbent for rhodamine B removal. *RSC Adv.* 7, 23255–23264. doi: 10.1039/C7RA03045B
- Molina-Sabio, M., and Rodriguez-Reinoso, F. (2004). Role of chemical activation in the development of carbon porosity. *Colloids Surfaces A Physicochem. Eng. Aspects* 241, 15–25. doi: 10.1016/j.colsurfa.2004.04.007
- Nisticò, R., Cesano, F., Franzoso, F., Magnacca, G., Scarano, D., Funes, I. G., et al. (2018). From biowaste to magnet-responsive materials for water remediation from polycyclic aromatic hydrocarbons. *Chemosphere* 202, 686–693. doi: 10.1016/j.chemosphere.2018.03.153
- Nisticò, R., Franzoso, F., Cesano, F., Scarano, D., Magnacca, G., Parolo, M., et al. (2017). Chitosan-derived iron oxide systems for magnetically-guided and efficient water purification processes from polycyclic aromatic hydrocarbons. *ACS Sustain. Chem. Eng.* 5, 793–801. doi: 10.1021/acssuschemeng.6b02126
- Pimenta, M. A., Dresselhaus, G., Dresselhaus, M. S., Cancado, L. G., Jorio, A., and Saito, R. (2007). Studying disorder in graphite-based systems by Raman spectroscopy. *Phys. Chem. Chem. Phys.* 9, 1276–1291. doi: 10.1039/B613962K
- Piñero-Prado, I., Salinas-Torres, D., Ruiz-Rosas, R., Morallón, E., and Cazorla-Amorós, D. (2016). Design of activated carbon/activated carbon asymmetric capacitors. *Front. Mater.* 3:16. doi: 10.3389/fmats.2016.00016
- Rahman, M. M., Cesano, F., Bardelli, F., Scarano, D., and Zecchina, A. (2010). Hybrid SnO₂/carbon composites: from foams to films by playing with the reaction conditions. *Catal. Today* 150, 84–90. doi: 10.1016/j.cattod.2009.07.063
- Rosas, J. M., Berenguer, R., Valero-Romero, M. J., Rodríguez-Mirasol, J., and Cordero, T. (2014). Preparation of different carbon materials by thermochemical conversion of lignin. *Front. Mater.* 1:29. doi: 10.3389/fmats.2014.00029
- Sadakane, M., Horiuchi, T., Kato, N., Sasaki, K., and Ueda, W. (2010). Preparation of three-dimensionally ordered macroporous perovskite-type lanthanum-iron-oxide LaFeO₃ with tunable pore diameters: High porosity and photonic property. *J. Solid State Chem.* 183, 1365–1371. doi: 10.1016/j.jssc.2010.04.012
- Sadakane, M., Sasaki, K., Nakamura, H., Yamamoto, T., Ninomiya, W., and Ueda, W. (2012). Important property of polymer spheres for the preparation of three-dimensionally ordered macroporous (3DOM) metal oxides by the ethylene glycol method: the glass-transition temperature. *Langmuir* 28, 17766–17770. doi: 10.1021/la303921u
- Shin, Y., Wang, L.-Q., Bae, I.-T., Arey, B. W., and Exarhos, G. J. (2008). Hydrothermal syntheses of colloidal carbon spheres from cyclodextrins. *J. Phys. Chem. C* 112, 14236–14240. doi: 10.1021/jp801343y
- Signorile, M., Bonino, F., Damin, A., and Bordiga, S. (2018). A novel Raman setup based on magnetic-driven rotation of sample. *Top. Catal.* 61, 1491–1498. doi: 10.1007/s11244-018-1033-z
- Sun, X., and Li, Y. (2005). Ag@C core/shell structured nanoparticles: controlled synthesis, characterization, and assembly. *Langmuir* 21, 6019–6024. doi: 10.1021/la050193+
- Sun, X. M., and Li, Y. D. (2004). Colloidal carbon spheres and their core/shell structures with noble-metal nanoparticles. *Angew. Chem. Int. Edn.* 43, 597–601. doi: 10.1002/anie.200352386
- Thommes, M., Kaneko, K., Neimark, A. V., Olivier, J. P., Rodriguez-Reinoso, F., Rouquerol, J., et al. (2015). Physisorption of gases, with special reference to the

- evaluation of surface area and pore size distribution (IUPAC Technical Report). *Pure Appl. Chem.* 87, 1051–1069. doi: 10.1515/pac-2014-1117
- Uddin, M. J., Daramola, D. E., Velasquez, E., Dickens, T. J., Yan, J., Hammel, E., et al. (2014). A high efficiency 3D photovoltaic microwire with carbon nanotubes (CNT)-quantum dot (QD) hybrid interface. *Phys. Status Solidi (RRL)-Rapid Res. Lett.* 8, 898–903. doi: 10.1002/pssr.201409392
- Wang, J. G., Liu, H., Sun, H., Hua, W., Wang, H., Liu, X., et al. (2018). One-pot synthesis of nitrogen-doped ordered mesoporous carbon spheres for high-rate and long-cycle life supercapacitors. *Carbon* 127, 85–92. doi: 10.1016/j.carbon.2017.10.084
- Wang, M., Wang, X., Yue, Q., Zhang, Y., Wang, C., Chen, J., et al. (2014). Templated fabrication of core-shell magnetic mesoporous carbon microspheres in 3-dimensional ordered macroporous silicas. *Chem. Mater.* 26, 3316–3321. doi: 10.1021/cm501186e
- Wollbrink, A., Volgmann, K., Koch, J., Kanthasamy, K., Tegenkamp, C., Li, Y., et al. (2016). Amorphous, turbostratic and crystalline carbon membranes with hydrogen selectivity. *Carbon* 106, 93–105. doi: 10.1016/j.carbon.2016.04.062
- Xu, F., Wu, D., Fu, R., and Wei, B. (2017). Design and preparation of porous carbons from conjugated polymer precursors. *Mater. Today* 20, 629–656. doi: 10.1016/j.mattod.2017.04.026
- Yang, D., Pang, X., He, Y., Wang, Y., Chen, G., Wang, W., et al. (2015). Precisely size-tunable magnetic/plasmonic core/shell nanoparticles with controlled optical properties. *Angew. Chem. Int. Edn.* 54, 12091–12096. doi: 10.1002/anie.201504676
- Yang, N., Zhu, S., Zhang, D., and Xu, S. (2008). Synthesis and properties of magnetic Fe₃O₄-activated carbon nanocomposite particles for dye removal. *Mater. Lett.* 62, 645–647. doi: 10.1016/j.matlet.2007.06.049
- Yi, J., Li, X. P., Hu, S. J., Li, W. S., Zhou, L., Xu, M. Q., et al. (2011). Preparation of hierarchical porous carbon and its rate performance as anode of lithium ion battery. *J. Power Sour.* 196, 6670–6675. doi: 10.1016/j.jpowsour.2010.12.017
- Yin, Y., Zhou, S., Min, C., and Wu, L. (2011). Preparation of rattle-type magnetic mesoporous carbon spheres and their highly efficient adsorption and separation. *J. Colloid Interface Sci.* 361, 527–533. doi: 10.1016/j.jcis.2011.05.014
- Zanetti, M., Anceschi, A., Magnacca, G., Spezzati, G., Caldera, F., Rosi, G. P., et al. (2016). Micro porous carbon spheres from cyclodextrin nanosponges. *Microporous Mesoporous Mater.* 235, 178–184. doi: 10.1016/j.micromeso.2016.08.012
- Zhang, H., Yan, Y., and Yang, L. (2010). Preparation of activated carbon from sawdust by zinc chloride activation. *Adsorpt. J. Int. Adsorpt. Soc.* 16, 161–166. doi: 10.1007/s10450-010-9214-5
- Zhang, J., Zhang, Y., Lian, S., Liu, Y., Kang, Z., and Lee, S.-T. (2011). Highly ordered macroporous carbon spheres and their catalytic application for methanol oxidation. *J. Colloid Interface Sci.* 361, 503–508. doi: 10.1016/j.jcis.2011.06.021

Conflict of Interest Statement: The authors declare that the research was conducted in the absence of any commercial or financial relationships that could be construed as a potential conflict of interest.

Copyright © 2019 Cesano, Cravanzola, Brunella, Damin and Scarano. This is an open-access article distributed under the terms of the Creative Commons Attribution License (CC BY). The use, distribution or reproduction in other forums is permitted, provided the original author(s) and the copyright owner(s) are credited and that the original publication in this journal is cited, in accordance with accepted academic practice. No use, distribution or reproduction is permitted which does not comply with these terms.